Subtidal Response of Scotian Shelf Circulation to Local and Remote Forcing. Part II: Barotropic Model

FRANKLIN B. SCHWING

Department of Oceanography, Dalhousie University, Halifax, Nova Scotia, Canada

(Manuscript received 29 August 1990, in final form 26 August 1991)

ABSTRACT

A linear, barotropic numerical model that features realistic bathymetry of the Scotian Shelf provides solutions forced by steady and periodic wind stress that are generally incoherent on spatial scales of the shelf width. Closed circulation cells occur in association with, and on the scales of, major bathymetric features. Bathymetrically steered flow is prevalent, and more evident at lower frequencies. Model transport forced by a coastally trapped wave propagating across the backward boundary is not sensitive to the modal structure of the incident wave; bathymetry rapidly modifies the wave form as it propagates in the free direction. Higher modes and reflected waves are probably dissipated over short distances by scattering and strong bottom stress. Patterns seen in the model solutions are consistent with results from more fundamental models, and are readily explained by relatively simple vorticity balances.

Model results generally reproduce the diverse local and nonlocal velocity responses observed on the Scotian Shelf during winter. The model is more effective in accounting for the remote contribution to circulation. Wind-forced results generally reflect the observed directional variability, and are similar in magnitude to observations inside the 100-m isobath but underestimate the actual current response at deeper stations. It is speculated that spatial variability in wind stress, an effect not addressed in this work, may be responsible for some of this difference. The significance of baroclinic effects in deeper water, which cannot be discounted, is also beyond the scope of this model. Nevertheless, the fairly good agreement between the model and observed current responses to local and nonlocal forcing confirms the importance of bathymetric modifications to Scotian Shelf circulation at subtidal frequencies.

1. Introduction

Winter storms crossing the coastal region of eastern Canada generate a systematic, well-defined response in subsurface pressure (SSP) on the continental shelf. Observations from the Canadian Atlantic Storms Program (CASP) on the Scotian Shelf show that over 90% of the subtidal energy in the SSP field is attributable to a combination of direct forcing by local wind stress and remote forcing by coastally trapped waves (CTWs) (Schwing 1989a,b). The SSP is set up (down) by the predominantly alongshelf stress to the east (west) in a response that is strongly coherent over the entire shelf. The magnitude of the locally forced response increases to the west (the forward or free direction) as the response diffuses away from the coast, consistent with Csanady's (1978) arrested topographic wave (ATW) theory. Changes in phase suggest propagation of the locally forced SSP signal to the west. Solutions to a harmonic time-dependent form of this model agree quite closely with the CASP observations (Schwing 1989b). The nonlocal contribution to SSP propagates and decays offshore and to the west, in quantitative agreement with frictional CTW theory for idealized Scotian Shelf bathymetry. The importance of remote forcing relative to local stress decreases to the west, as CTW modes are reflected, scattered, and frictionally decay while the local response grows in the forward direction.

However, subtidal current fluctuations on the Scotian Shelf are less coherent in space, and with local and remote meteorological forcing (Schwing 1989a, 1992). The large-scale observed current response reflects some of the features noted in the SSP field, although considerable variations occur within the mooring array on horizontal scales of less than 100 km. The discrepancy between the velocity and SSP coherence scales is similar to that observed by Vermersch et al. (1979) in the nearby Gulf of Maine. They suggest that mesoscale variations in bottom bathymetry, similar to those occurring on the Scotian Shelf, induce current variability on the same scale. Webster and Narayanan (1988) attribute differences between model results and observations on the Labrador Shelf to bathymetric irregularities.

Numerous idealized analytical (Csanady 1974; Wilkin and Chapman 1987; Middleton and Wright

Corresponding author address: Dr. Franklin B. Schwing, National Marine Fisheries Service/NOAA, Pacific Fisheries Environmental Group, Southwest Fisheries Science Center, P.O. Box 831, Monterey, CA 93942.

1988) and numerical (Wang 1980; Simons 1983; Brink 1986; Haidvogel and Brink 1986; Wilkin and Chapman 1990) studies have demonstrated a link between complex circulation features and bathymetric structures. Other theoretical studies that considered more realistic bottom geometries display a similar flow/bathymetry relationship (Hsueh 1980; Beardsley and Haidvogel 1981; Hopkins and Dieterle 1983; Wright et al. 1986; Greenberg and Petrie 1988; Lynch et al. 1992). A series of simple analytical and numerical model simulations by Schwing (1989a) demonstrate that a highly variable velocity field develops over irregular bathymetry, primarily because of small-scale circulation features created by bathymetric steering, vortex stretching, and the scattering of wave energy by bathymetric features. The velocity response observed during CASP cannot be reconciled with the simple model applied to SSP (Schwing 1989b).

To relate these fundamental model results back to the CASP observations detailed in Schwing (1992), numerical techniques are applied here to the problem of locally and remotely forced flow on the Scotian Shelf, using actual bathymetric data for the region. Solutions are compared with observations to verify how well these models explain the balance of forces that control subtidal flow, with emphasis on the role of complex bathymetry. Model results for idealized bathymetric examples will aid in the interpretation of the more realistic case studies described here. In addition, model results from remote portions of the Scotian Shelf will serve as a reference frame for future observational studies. Finally, it is hoped that these results will provide further insight on the proper remote forcing for Gulf of Maine, Georges Bank, and Middle Atlantic Bight models. Chapman et al. (1986) conclude that the observed mean flow in the Middle Atlantic Bight may be driven strictly by inflow from the Scotian Shelf.

In section 2, the numerical model is derived, and the bathymetric mesh and boundary conditions for the Scotian Shelf models are described. Model results forced by wind stress over the shelf are presented in section 3. The nonlocal contribution, driven by a CTW incident at the backward (eastern) cross-shelf boundary, is discussed in section 4. The observed velocity response to these sources of energy, discussed in Schwing (1992), is compared to model currents as well. A discussion of these results, and their limitations, follows in section 5.

2. The numerical model

a. Derivation of the governing equation

A governing equation is sought in terms of sea surface elevation η from the two-dimensional linear, shallow-water, barotropic equations of motion and continuity:

$$i\omega u - fv = -g\eta_x + \frac{\tau^x}{h} - \frac{ru}{h} \tag{1}$$

$$i\omega v + fu = -g\eta_y + \frac{\tau^y}{h} - \frac{rv}{h} \tag{2}$$

$$i\omega\eta + (uh)_x + (vh)_y = 0, \tag{3}$$

where u, v are depth-averaged cross-shelf (x) and alongshelf (y) components of velocity, respectively; τ^x, τ^y are kinematic wind stress components in the cross- and alongshelf directions, respectively; f is the (constant) Coriolis parameter; g is the acceleration due to gravity; h is the water depth; and r is the linear bottom stress coefficient. Subscripts denote partial differentiation. The right-handed coordinate system (Fig. A1) defines $x = 0$ at the coast and increasing offshore; y becomes increasingly negative in the direction of free wave propagation (i.e., forward). Harmonic time dependence of the form $e^{i\omega t}$ is assumed for all time derivatives, where ω is the frequency of forcing.

Equations (1)–(2) give equations for the current components

$$u = \frac{1}{1+\epsilon^2}\left[-\frac{g}{f}(\epsilon\eta_x + \eta_y) + \frac{1}{fh}(\tau_y + \epsilon\tau^x)\right] \tag{4}$$

$$v = \frac{1}{1+\epsilon^2}\left[\frac{g}{f}(\eta_x - \epsilon\eta_y) + \frac{1}{fh}(\epsilon\tau^y - \tau^x)\right], \tag{5}$$

where

$$\epsilon = i\frac{\omega}{f} + \frac{r}{fh}. \tag{6}$$

Now substituting (4)–(6) into (3) yields the governing equation

$$\frac{a^2\epsilon}{1+\epsilon^2}(\nabla^2\eta) + \left[\left(\frac{a^2\epsilon}{1+\epsilon^2}\right)_x - \left(\frac{a^2}{1+\epsilon^2}\right)_y\right]\eta_x + \left[\left(\frac{a^2}{1+\epsilon^2}\right)_x + \left(\frac{a^2\epsilon}{1+\epsilon^2}\right)_y\right]\eta_y - i\frac{\omega}{f}\eta = \frac{1}{f^2}\left[\left(\frac{\tau^y + \epsilon\tau^x}{1+\epsilon^2}\right)_x + \left(\frac{\epsilon\tau^y - \tau^x}{1+\epsilon^2}\right)_y\right], \tag{7}$$

where $a^2 = gh/f^2$. Equation (7) is an elliptic partial differential equation expressed solely in terms of the variable η, but is not readily solved with analytical techniques. Various assumptions and approximations may be applied to (1)–(3) to reduce (7) to an equation that can be solved analytically (cf. Wilkin and Chapman 1987; Middleton and Wright 1988).

Alternatively, a numerical approximation can be applied. The discretization of (7), and its solution using successive overrelaxation (SOR), a point-iterative, explicit method (Young 1971, p. 73ff.; Press et al. 1986, pp. 652–659), is discussed in appendix A. An advantage of relaxation schemes over other numerical techniques is that the matrix of coefficients **A**, given by (A4), is not altered during computations. Thus, the problem of accumulation of round-off errors experi-

enced by many direct methods, such as Gaussian elimination, can be avoided. SOR is also extremely efficient because 1) only nonzero values of **A**, a very small percentage of the elements, are stored, 2) values of the solution are updated in place, as they become available during the iteration, and 3) a relaxation parameter α is applied to overcorrect, in the case of $\alpha > 1$, the initial solution, which leads to more rapid convergence to the final solution (Young 1971, pp. 73–74). The convergence rate for SOR provides three-figure accuracy after about N iterations, where N is the number of model elements. Details of the discretization scheme are given in Fig. A1.

b. The model bathymetry

Model bathymetry (Fig. 1), supplied by Sylvain de Margerie (ASA Consulting, Ltd., Halifax, Nova Scotia), was developed from a database of existing depth soundings for the Scotian Shelf and adjacent areas. Observations were averaged into 10-km by 10-km elements. The coastline was smoothed to simplify the boundary, the coastal depth was set to 10 m, and land regions were masked. The cross-shelf resolution was then doubled to 5 km by interpolation. The final bathymetric dataset used in the numerical model contains 59 points cross-shelf and 88 values alongshelf, corresponding to a 290- by 870-km domain. Major bathymetric features and the approximate locations of CASP stations are indicated in Fig. 1.

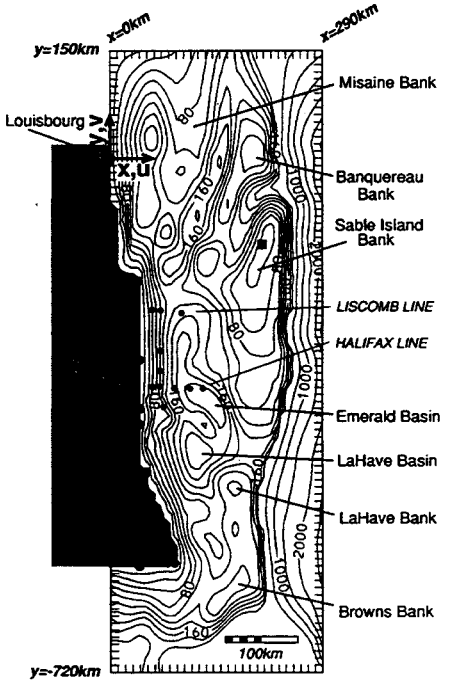

FIG. 1. Domain and bathymetry used in Scotian Shelf numerical model simulations. Model mesh is 290 km wide and 870 km in length. The 10-km resolution is denoted by the tick marks. Approximate position of Nova Scotia shown by shaded area. Location of major bathymetric features is indicated. Approximate position of CASP coastal and offshore stations denoted by solid circles. Larger circle denotes Louisbourg (model origin). Square denotes location of Sable Island meteorological station.

The backward (relative to the direction of free wave propagation) cross-shelf boundary ($y = 150$ km) was set to the exponential form

$$h(x) = h_L \exp[2b(x - L)]$$

over the region $0 < x < L$, where $h_L = 200$ m, $bL = 0.35$, and $L = 230$ km, the approximate offshelf position of the 200-m isobath in this region. These depths were smoothed linearly into the actual bathymetry at the origin (Louisbourg), over the alongshelf distance $0 < y < 150$ km. The cross-shelf structure of any CTW mode can be determined analytically for the profile at this boundary (cf. Wilkin and Chapman 1987; Middleton and Wright 1988), as described in appendix B. The incident wave then adjusts to the actual bathymetry over the "patched" section east of Louisbourg. This patched region is rather complicated in reality. However, the model is not sensitive to the form of bathymetric transition, and the model circulation in this region is not crucial to the interpretation of the CASP observations.

Finally, the depth matrix was smoothed with a weighted 3×3 spatial filter:

$$h_{i,j}^{\text{smoothed}} = (h_{i+1,j} + h_{i+1,j+1} + h_{i,j+1} + h_{i-1,j+1} + h_{i-1,j} + h_{i-1,j-1} + h_{i,j-1} + h_{i+1,j-1} + 5h_{i,j})/13,$$

where the subscripts denote the mesh point, as defined in Fig. A1. The filter was applied three times to interior points in the matrix. Some areas were further smoothed to avoid model instabilities where the depth gradient is too severe, given the $\Delta x = 5$ km cross-shelf and $\Delta y = 10$ km alongshelf interval between mesh points.

c. Boundary conditions

Along the coastal boundary ($y > -570$ km, Fig. 1), transport normal to the coast must be zero. The condition at mesh points where the coastline is oriented parallel to the y axis is obtained from (4), assuming $uh_0 = 0$, where h_0 is the nonzero depth and ϵ_0 is ϵ, evaluated at the coast:

$$\eta_x + \epsilon_0^{-1}\eta_y - \frac{\tau^x}{gh_0} - \frac{\tau^y}{\epsilon_0 gh_0} = 0. \qquad (8a)$$

At coastal points where the coastline orientation is parallel to the x axis, the requirement that $vh_0 = 0$ is combined with (5) to give

$$\eta_y - \epsilon_0^{-1}\eta_x + \frac{\tau^x}{\epsilon_0 gh_0} - \frac{\tau^y}{gh_0} = 0. \qquad (8b)$$

All the terms in (8) are of similar order for typical coastal depths $h_0 = O(10\text{ m})$. Csanady (1980) elaborates on this condition, and justifies the need for $h_0 \neq 0$.

The offshore alongshelf boundary condition

$$\eta = 0 \tag{9}$$

is applied seaward of the 200-m isobath at the shelf break. It is based on the assumption that synoptic variations in η over the continental slope and deeper regions are negligible (Beardsley and Haidvogel 1981; Wright et al. 1986). Transport onto the shelf must be conserved. To compensate for the large decrease in depth, the depth-integrated cross-isobath velocity must be small compared to u on the outer shelf. Since flow in the deep ocean is nearly geostrophic, $\eta_y \approx 0$ at the ocean boundary and η can be approximated as a constant (Hsueh 1980; Beardsley and Haidvogel 1981; Hopkins and Dieterle 1983; Wright et al. 1986).

This assumption eliminates the need for computations in the shelf slope region, where the depth gradient is too severe to allow stable solutions given a mesh size sufficiently large to keep computing times at a reasonable length. Results from sensitivity studies, using various idealized forms of bathymetry in the offshelf region and applying condition (9) at the outer alongshelf boundary of the domain, suggest that prescribing sea level to zero along the shelf break has only minor effects on shelf SSP and transport. Furthermore, these effects are confined to within a few mesh points of the break.

Hsueh (1980) and Hopkins and Dieterle (1983) discuss some of the limitations of this approximation. Hopkins and Dieterle treat the distribution of η_y, necessary to solve the backward boundary condition, as the sum of two gradients that decay away from the coast and the shelf break. These can be thought to be forced by local wind stress and the deep ocean, respectively. The total shelf circulation therefore could be separated into three contributions: local wind forcing and remote forcing across the backward boundary, as applied here, plus remote forcing from offshore. The effects of the last component are beyond the scope of this study, but are probably minimal. Chapman et al. (1986) conclude that relatively little exchange occurs across the shelf break in the area just west of the Scotian Shelf.

The condition

$$\eta_{yy} = 0 \tag{10a}$$

applied at the forward (relative to the direction of free wave propagation) cross-shelf boundary ($y = -720$ km) allows flow out of the domain to compensate for mass divergence in the interior (Hsueh 1980; Hopkins and Dieterle 1983). A concern of those studies is that (10a) may be overprescribed if the second derivative of η is small throughout the interior. Given the short bathymetric scales in y on the Scotian Shelf, however, this condition is appropriate. Similarly,

$$\eta_{xx} = 0 \tag{10b}$$

is applied along the open portion of the $x = 0$ boundary west of Nova Scotia; that is, $y < -570$ km (Fig. 1).

Before describing the backward cross-shelf boundary conditions for the local and remote models, an explanation of how they were treated is in order. Schwing's (1992) analysis of the CASP observations separates the circulation into locally and remotely forced portions, based on a concept suggested by Gill and Schumann (1974) and others (cf. Lopez and Clarke 1989). The locally forced contribution is due to wind stress over the Scotian Shelf and, by definition, must be zero at some cross-shelf section near the eastern edge of the shelf. The structure of η at the origin ($y = 0$) represents the accumulated transport onto the Scotian Shelf, and is a function of the forcing and bathymetric conditions in the backward region (Hopkins and Dieterle 1983). For the Scotian Shelf model, I prescribe $\eta = 0$ at Louisbourg, near the Laurentian Channel (Fig. 1), an appropriate condition if little wind-forced variation in SSP traverses this deep channel. The remote portion of velocity is defined by the total SSP signal measured at Louisbourg, regardless of its source and structure. Another physical interpretation of this solution is that the remote contribution is due to a (primarily low-mode) pressure gradient force, while the local (higher-mode) response is dependent on direct wind stress (Lopez and Clarke 1989).

Since η must match at the junction of the offshore and cross-shelf boundaries, condition (9) is also applied at $y = 0$ for the periodic wind-forced cases (section 3). This is a critical prescription, as it assumes the SSP signal at this boundary is associated solely with motions generated remote from the shelf. As Wright et al. (1986) have pointed out, the observed response is highly sensitive to changes in this condition. Thus, solutions to (7) subject to (9) at $y = 0$ represent only that portion of SSP forced by *local* wind stress (i.e., directly over the model domain); nonlocally generated motions are excluded from the solution.

The nonlocal contribution to the circulation (section 4) is forced at the backward boundary ($y = 150$ km) by a single-mode CTW. This condition is determined analytically by calculating the cross-shelf modal streamfunction for the exponential bottom profile (see appendix B). The cross-shelf structure of the incident wave, expressed in terms of η, is found by integrating the y-momentum equation (2) with respect to y, after substituting the constant Rayleigh damping coefficient $\lambda = r/h_0$ and the streamfunction Ψ (described in appendix B). Thus,

$$\eta(x) = \frac{f}{gh}\left[\Psi(x) + \frac{\epsilon}{il^2}\Psi_x(x)\right], \tag{11}$$

plus a constant of integration that reduces η to zero at the 200-m isobath to match (9) at the offshore boundary. Although the rigid-lid assumption is required to

obtain condition (11), it is relaxed in the interior of the model.

The numerical model was tested by forcing an incident low-mode CTW over various cross-shelf exponential, uniform alongshelf bathymetries. Solutions exhibited the phase speeds and exponential amplitude decay scales identical to analytical solutions of Eq. (B1) for the appropriate bathymetric scale and bottom friction coefficient (Schwing 1989a). Subsequent experience with the model (discussed in the following sections) revealed that the sea surface structure at the backward boundary is unimportant in model flow patterns over realistically complex bathymetry. The role of (11) is to force the model with a cross-shelf sea level setup, analogous to the remote contribution defined by Schwing (1992), and shown to be important by Beardsley and Haidvogel (1981), Chapman et al. (1986), Wright et al. (1986), and Lynch et al. (1992). It does not necessarily represent a CTW signal at Louisbourg, nor is it applied for the purposes of describing the remotely forced portion of the Scotian Shelf circulation in terms of a CTW modal structure.

The coastal (8), offshore (9), and forward (10) boundary conditions for the remotely forced problem are identical to those applied to the wind-forced case, although the wind stress terms in (8) are zero for the remote simulations. Sensitivity studies with a nonlocally forced streamfunction model using the cross-shelf radiation conditions for long and short CTWs (cf. Wang 1980) produced essentially identical results to that using (10)–(11).

Bottom stress is parameterized by setting it proportional to the depth-averaged velocity (Csanady 1980). The coefficient $r = 10^{-3}$ m s^{-1} for all model results presented here, consistent with values derived empirically from observations and used in other shelf models (cf. Csanady 1978, 1982, pp. 185–186). Sensitivity studies indicate that this value of r provides the best reproduction of the SSP response at CASP coastal and mooring stations. These studies also show that decreasing r from 10^{-3} to 2×10^{-4} m s^{-1} raises the coastal SSP response by less than 20%, and has even less effect on the response farther offshore. The circulation features of note are not qualitatively affected by reasonable changes in r.

3. Model results for local wind stress forcing

a. Response to the mean wind field

The initial numerical model results are forced by a spatially uniform, steady ($\omega = 0$) wind stress over the entire domain (Fig. 2). The magnitude of the model stress is the record mean of the Sable Island wind stress time series during CASP; the alongshelf component ($\tau^y = 0.0436$ Pa) dominates the cross-shelf contribution ($\tau^x = 0.0132$ Pa). For clarity, all flow fields are presented at a 10-km resolution.

Transport near the coast is predominantly along isobath and toward the east. Although isobaths, hence transport, are generally parallel to the coast, even small bathymetric deviations can produce sizable cross-shelf flow. This is most apparent off Halifax, which is coincidently very close to the CASP array (Fig. 1). Transport also generally increases in the direction of free wave propagation, consistent with the increased setdown of SSP seen in the CASP observations and idealized model results (Schwing 1989a,b), and according to ATW theory (Csanady 1978).

Transport near the eastern boundary and over the outer shelf banks (e.g., Sable Island Bank) is predominantly offshelf, consistent with the direction of a surface Ekman flux for the mean wind. Compare the transport in these regions to that seaward of the 200-m isobath, where the current is solely a surface Ekman response.

Over the deeper portions of the outer shelf, however, the circulation is not nearly as simple. Flow through the saddle region separating Sable Island and La Have banks, and in the small canyon east of Sable Island, features a relatively strong *onshelf* transport that balances a large pressure gradient, despite the offshelf favorable stress. These results suggest that slope water upwelled onto the shelf (Petrie 1983) may be transported into Emerald Basin during winter, even in the absence of stratification. Onshelf barotropic flow may account in part for the anomalously high proportion of intermediate slope water found during CASP within the deeper layers of Emerald Basin (Anderson and Smith 1989).

While transport is greatest through the aforementioned saddle region, the strongest depth-averaged velocity is generally confined inside the 100-m isobath and over Sable Island Bank (Fig. 2b). This is not surprising, since the response to surface and bottom stress is most efficient in the shallowest regions of the shelf.

The final noteworthy feature of the steady results is the existence of several circulation cells about 50–100 km in diameter, located in the deeper areas of the shelf where depth gradients are strongest (e.g., along the slopes of La Have Basin). These cells are very similar in appearance to those noted in idealized bathymetric cases, whose origin was shown to be due to vortex stretching (Schwing 1989a). The rather small horizontal coherence scales are also consistent with the time-dependent current patterns observed during CASP (Schwing 1992).

The mean flow displays features of the steady, wind-forced solutions for the Gulf of Maine numerical models of Wright et al. (1986) and Lynch et al. (1992), which include the western portion of the Scotian Shelf. Their results include the pattern expected by ATW theory, a strong tendency for flow along depth contours, and several areas of closed, bathymetrically controlled circulation. Both studies also noted transport into Northeast Channel, opposite the surface Ekman trans-

port but consistent with the winter observations of Ramp et al. (1986). Wright et al. determined that flow in this channel is nearly geostrophic. An analysis of the steady momentum balance near Sable Island Bank provides a similar conclusion.

b. *Response to periodic wind stress forcing*

Multiple linear regression models in the frequency domain were applied by Schwing (1989b, 1992) to determine the local and remote contributions to the circulation. The regression analysis separates the flow into a response to the two wind stress components, and to a nonlocally forced signal represented by Louisbourg SSP. Model results presented in this section describe the velocity response to alongshelf and cross-shelf wind stress periodic at 0.125 and 0.438 cpd. The wind stress amplitude is 1 Pa over the shelf forward of Louisbourg, but zero in the region east of Louisbourg. Thus, numerical solutions can be compared directly to the statistical results from Schwing (1992), where the velocity signal at the cross-shelf transect off Louisbourg was defined as the nonlocal contribution to the flow.

Model transport forced by an alongshelf stress periodic at 0.125 cpd is presented at $t = 0$, when stress is at its maximum to the east (Fig. 3a), and at $t = \pi/2$, when the wind is relaxed after a half period ($-\pi/2 < t < \pi/2$) of eastward-directed stress (Fig. 3b). Transport

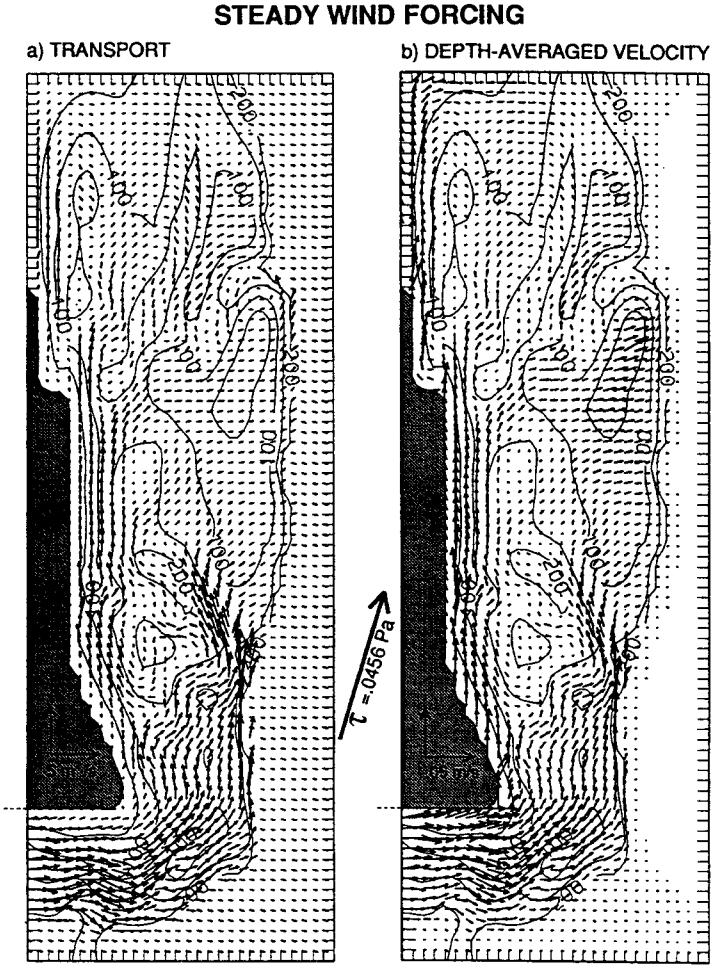

FIG. 2. Model circulation for Scotian Shelf, for mean wind stress during the CASP field deployment. Transport shown in (a); depth-averaged velocity shown in (b). Vector units are $m^2 s^{-1}$ and $m s^{-1}$, respectively. White areas denote velocity less than 0.0005 $m s^{-1}$.

amplitude is expressed in units of $m^2\ s^{-1}/Pa$. The flow field at $t = 0$ looks much like that due to a steady wind stress (Fig. 2a), with significant variability on the horizontal scales of, and in association with, bathymetric features.

The weak transport in the region east of Louisbourg gives an indication of how rapidly reflected (shortwave) energy is dissipated over the rugged terrain of the Scotian Shelf. Bathymetry acts to reflect waves or scatter their energy into higher modes (Wang 1980; Wilkin and Chapman 1987, 1990; Middleton and Wright 1988). Realistic shelf geometries scatter significant levels of wave energy into higher modes (Wilkin and Chapman 1990). The resulting waves dissipate more rapidly than the forward-propagating incident wave (Schwing 1989a).

Since transport is nearly in phase with wind forcing, the flow is weak over most of the domain at $t = \pi/2$ (Fig. 3b). However, a rather substantial residual circulation exists in the two basins off Halifax, and over the western part of the shelf. As with the flow at $t = 0$ and the steady forcing case, mesoscale circulation features of order 100 km and less in diameter occur at several locations. Such features are intimately associated with bathymetric features having similar horizontal scales.

The amplitude of the current response to τ^x, the cross-shelf wind stress (Fig. 4), is smaller than the response to the alongshelf component of stress. Wright et al. (1986) also noted this in their (steady) Gulf of Maine model results. Since the winter wind on the Scotian Shelf is predominantly alongshelf, the contribution to the circulation by τ^x is minor. An offshore wind stress at $t = 0$ results in a generally westward transport (Fig. 4a), consistent with the surface Ekman flux produced by such a wind. Some bathymetric steering is again evident, although not to the same degree as was noted for the τ^y response. Bathymetric effects on the flow are more obvious at $t = \pi/2$, when the wind is shifting to an onshore direction. In general, however, the circulation driven by cross-shelf wind stress is coherent on large horizontal scales relative to the response to alongshelf forcing.

The shelf-scale patterns reflected in the response to τ^y (Fig. 5) and τ^x (Fig. 6) at 0.438 cpd are similar to those occurring at lower frequencies. However, mesoscale variations are not nearly as apparent in the synoptic band. Secondary circulation characteristics are most significant when τ^y is weak (Fig. 5b), but otherwise the flow exhibits a strong alongshelf tendency, with an appropriate surface Ekman adjustment. As the frequency of forcing increases, the relative importance of bathymetric steering is reduced. A similar trend has been noted for model runs featuring idealized bathymetric changes (cf. Haidvogel and Brink 1986; Schwing 1989a). Again the response to cross-shelf wind forcing (Fig. 6) is spatially coherent over larger scales than is the τ^y response.

c. Comparison with observations

The cross-shelf component of wind stress during CASP was relatively small, and the observed current response to it was generally weak (Schwing 1992). Model solutions suggest that this response is relatively uniform in space and that the resulting flow is primarily alongshelf. In addition, the observed τ^x response was confined near the surface. Therefore, comparisons between depth-averaged velocity calculated from numerical model results and those determined from regression analysis of the observations are limited to the alongshelf stress response.

The model velocity field in the CASP region is compared to the observed surface and deeper flows at 0.125 cpd (Fig. 7) and 0.438 cpd (Fig. 8). Model circulation is represented by the lighter vectors. The observed near-surface (<50-m depth) velocity response is denoted by the heavy solid vectors, and the deeper response by broken vectors. Observations are representative of all instruments at a mooring, and are usually given for the meters most coherent with wind stress.

Near-surface observations display a systematic anticyclonic rotation from model results, while currents below 50 m are oriented cyclonically relative to the model. This is due in part to the fact that the model provides an estimate of the depth-averaged velocity, while observations were obtained at discrete depths. The model, of course, implicitly includes surface and bottom Ekman spirals in the parameterization of stresses, although the vertical structure of the current does not appear in the solutions. A barotropic depth-variable model of the western Scotian Shelf (Lynch et al. 1992) shows little velocity change with depth; however, flow in the bottom Ekman layer veers cyclonically. The direction of the depth-integrated transport, determined from the observed responses, is more consistent with model results.

In general, variations in the direction of flow implied by the observed velocity responses are reproduced in the model solutions. Flow at stations inside the 100-m isobath near Halifax exhibits a very strong eastward, primarily alongshelf flow. The current at the Liscomb line was predominantly offshelf, as predicted by the model. The observed velocity in Emerald Basin and west of the Halifax line is also consistent with the more variable, bathymetrically controlled circulation suggested by the model in these regions. For example, the westward flow at 0.125 cpd (Fig. 7b) and onshelf flow at 0.438 cpd (Fig. 8b) at the deepest station (S4) are reproduced. The observed and model current magnitudes are also fairly comparable near the coast. However, the velocity responses at stations beyond the 100-m isobath are rather large relative to model estimates.

Observed (solid vectors) and modeled (broken vectors) alongshelf velocity and SSP responses to τ^y are compared in Fig. 9, using the Argand diagrams introduced in Schwing (1992). A consideration of the

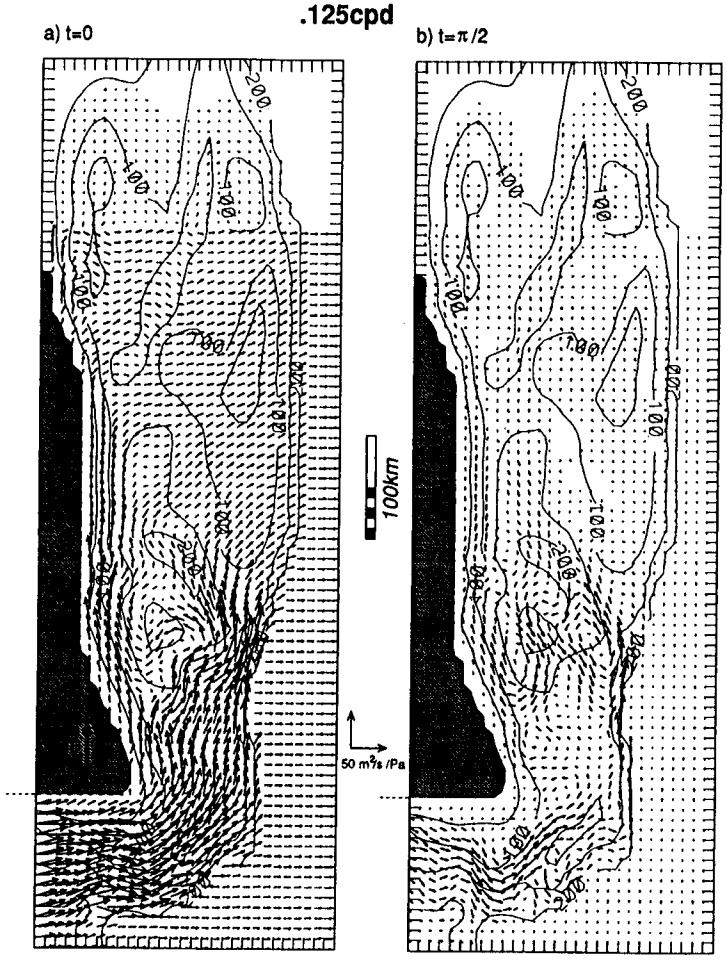

FIG. 3. Model response of transport to alongshelf wind stress, at 0.125 cpd. Wind field is zero backward of Louisbourg ($0 < y < 150$ km), and 1 Pa forward of Louisbourg. Transport shown at (a) $t = 0$ and (b) $t = \pi/2$. Vector units are $m^2\ s^{-1}/Pa$. White areas denote transport less than 1 $m^2\ s^{-1}/Pa$.

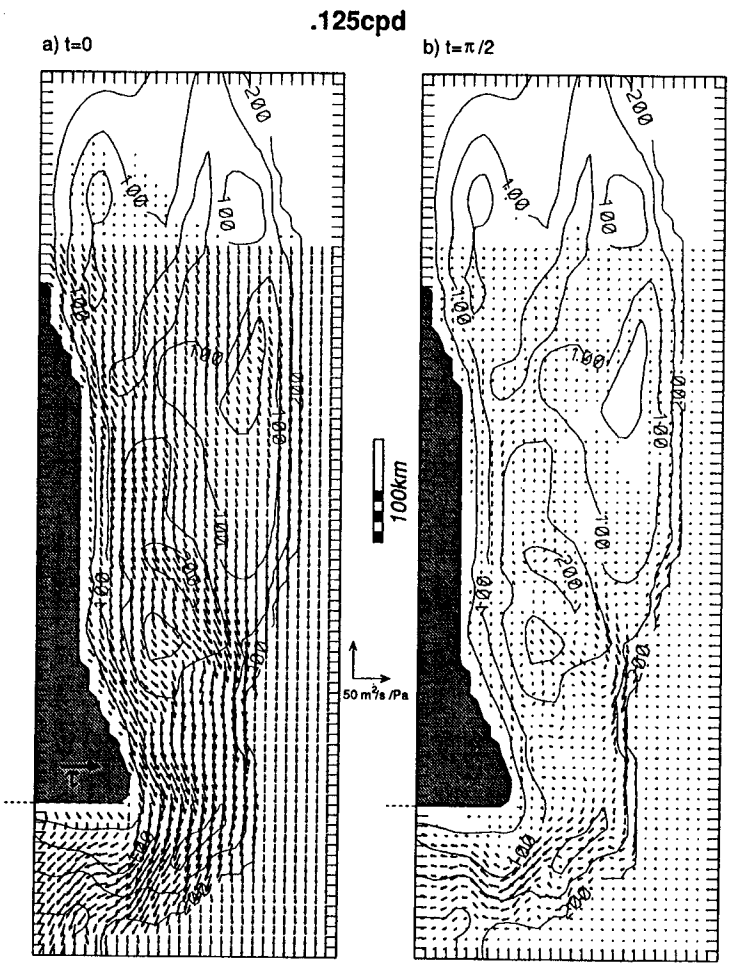

FIG. 4. Model response of transport to cross-shelf wind stress, at 0.125 cpd. Wind field is zero backward of Louisbourg and is 1 Pa forward of Louisbourg. Transport shown at (a) $t = 0$ and (b) $t = \pi/2$. Vector units are $m^2\ s^{-1}/Pa$. White areas denote transport less than 1 $m^2\ s^{-1}/Pa$.

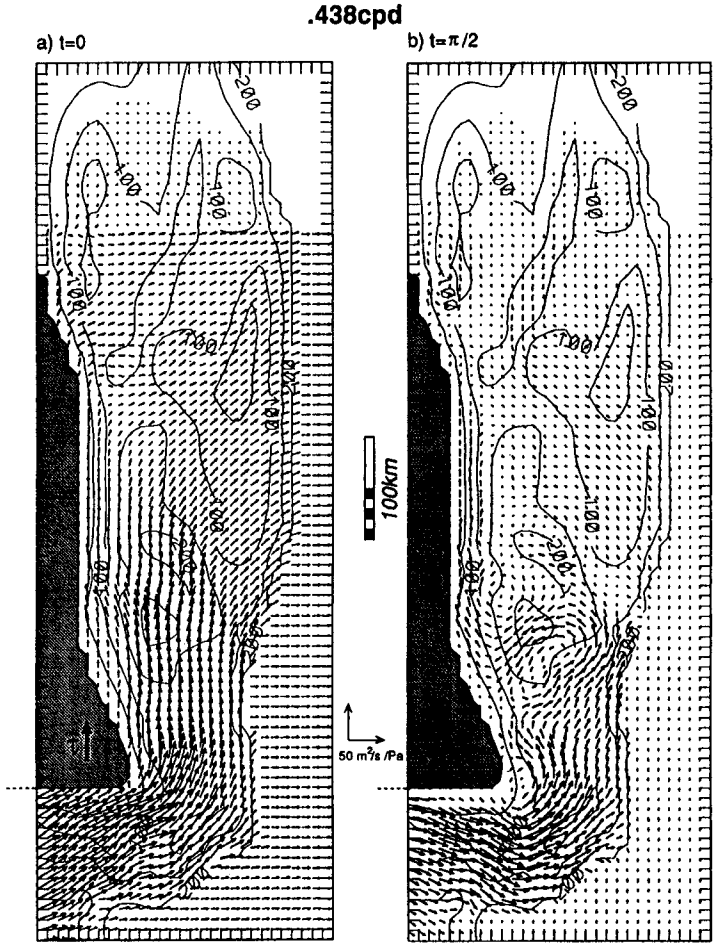

FIG. 5. Model response of transport to alongshelf wind stress, at 0.438 cpd. Wind field is zero backward of Louisbourg and 1 Pa forward of Louisbourg. Transport shown at (a) $t = 0$ and (b) $t = \pi/2$. Vector units are $m^2\ s^{-1}/Pa$. White areas denote transport less than $1\ m^2\ s^{-1}/Pa$.

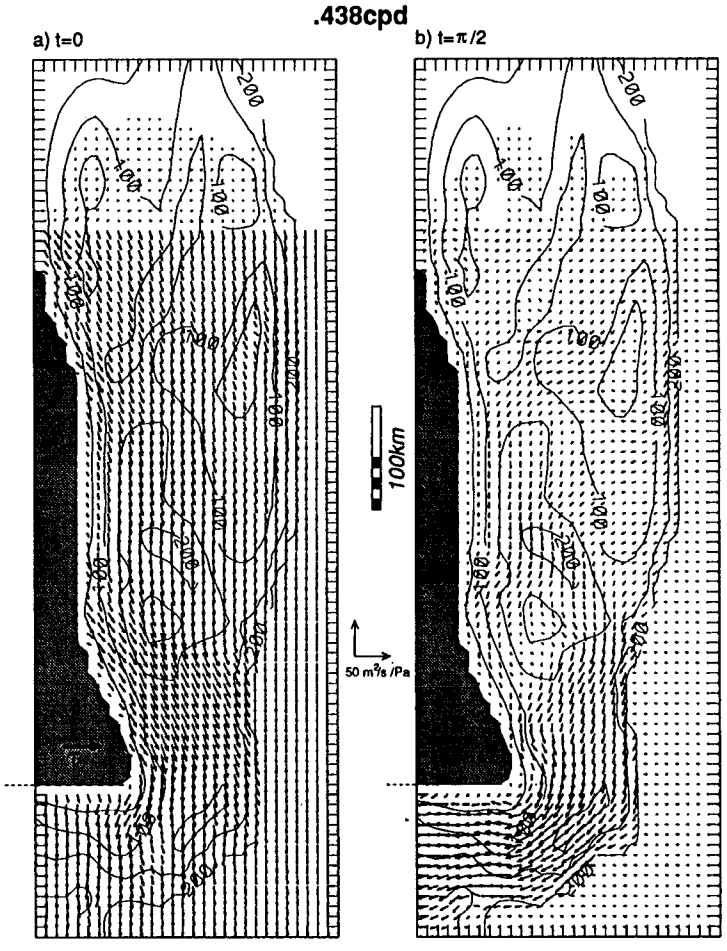

FIG. 6. Model response of transport to cross-shelf wind stress, at 0.438 cpd. Wind field is zero backward of Louisbourg and 1 Pa forward of Louisbourg. Transport shown at (a) $t = 0$ and (b) $t = \pi/2$. Vector units are $m^2\ s^{-1}/Pa$. White areas denote transport less than $1\ m^2\ s^{-1}/Pa$.

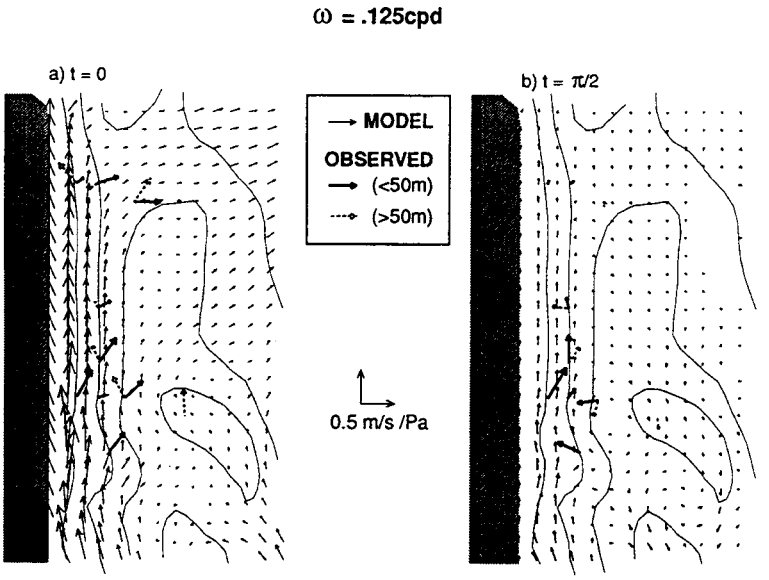

FIG. 7. Comparison of observed velocity to model results, for 1 Pa periodic alongshelf wind stress forcing at 0.125 cpd, at (a) $t = 0$ and (b) $t = \pi/2$. Results are expressed in units of m s^{-1}/Pa. Model velocity denoted by lighter vectors. Observed near-surface (<50 m) velocity at CASP moorings denoted by bold vectors, deeper (>50 m) velocity denoted by broken vectors. Observations based on typical transfer response determined by multiple regression analysis in Schwing (1992).

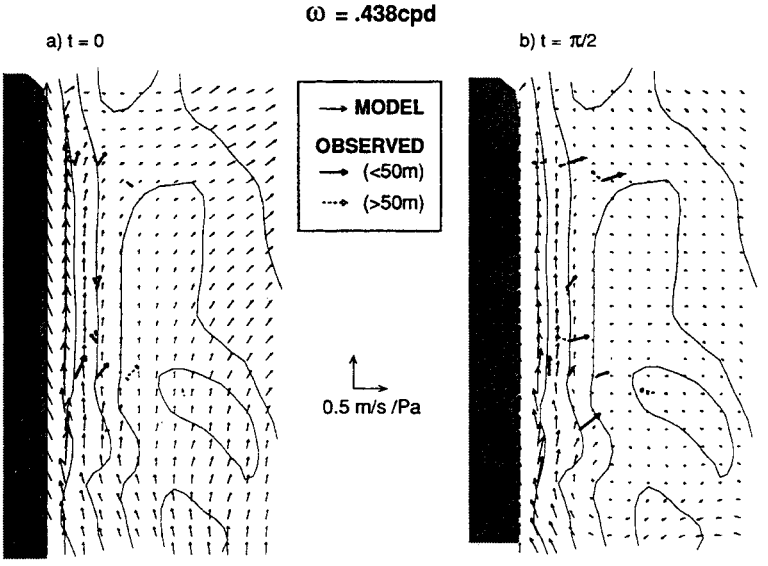

FIG. 8. Comparison of observed velocity to model results, for 1 Pa periodic alongshelf wind stress forcing at 0.438 cpd, at (a) $t = 0$ and (b) $t = \pi/2$. Results are expressed in units of m s^{-1}/Pa. Model velocity denoted by lighter vectors. Observed near-surface (<50 m) velocity at CASP moorings denoted by bold vectors, deeper (>50 m) velocity denoted by broken vectors. Observations based on typical transfer response determined by multiple regression analysis in Schwing (1992).

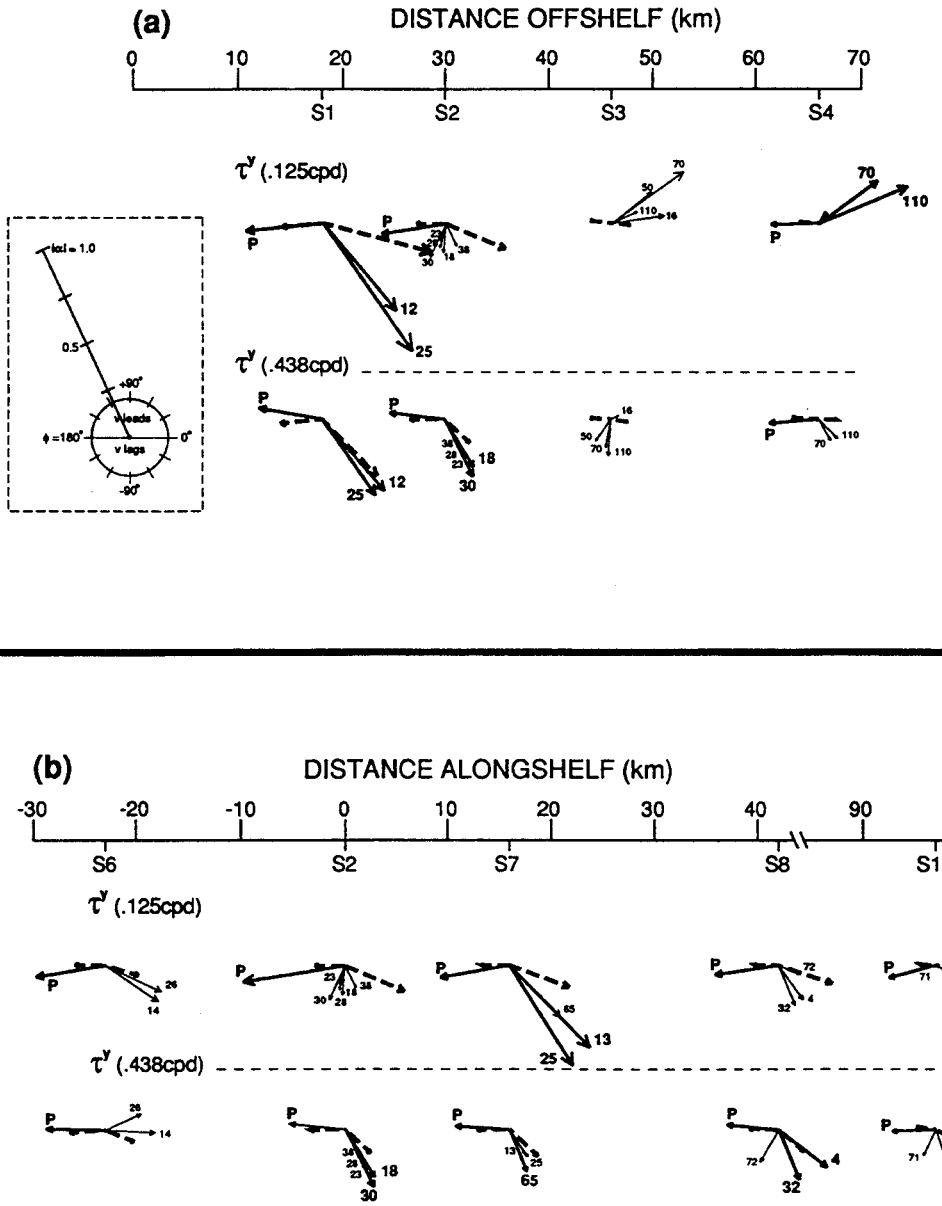

FIG. 9. Comparison of observed and model responses of v to alongshelf wind stress forcing at 0.125 and 0.438 cpd, for stations in the (a) Halifax line and (b) 100-m isobath line. Vectors describe amplitude and phase of response. Model results (broken vectors) adapted from Figs. 3 and 5. Observations (solid vectors) based on multiple regression analysis of Schwing (1992); bold vectors denote 95% significance.

alongshelf current alone shows that the model estimate of that component is somewhat better. The observed alongshelf response is fairly uniform with depth, in contrast with the cross-shelf velocity component. However, the amplitude of v at stations beyond the 100-m isobath is still underestimated by a factor of 2 or more, particularly at 0.125 cpd. The stronger flow at $t = \pi/2$ (Figs. 7b and 8b) is due in part to larger phase differences between the measured current and τ^y than the model suggests. The model typically leads

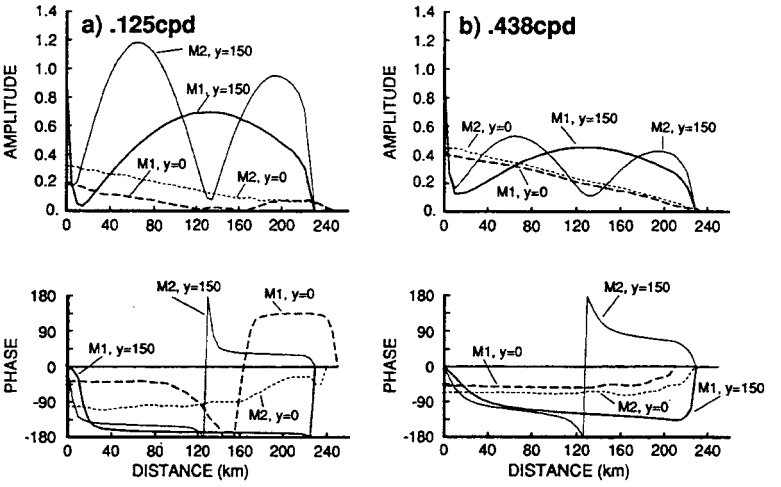

FIG. 10. Model amplitude and phase of SSP at backward cross-shelf boundary (y = 150 km) and transect off Louisbourg (y = 0) at (a) 0.125 cpd and (b) 0.438 cpd. Solutions are forced by mode 1 (M1) or mode 2 (M2) incident CTW at y = 150 km. Amplitude normalized by coastal SSP at origin. Phase in degrees relative to origin. Cross-shelf distance relative to coast.

observations by 10–15 h at 0.125 cpd, and 3–6 h at 0.438 cpd.

Although the model and observed SSP phases at the CASP moorings in both frequency bands agree within about 2–3 h, the observed SSP amplitude is again about twice that of the model (Fig. 9). Coastal SSP magnitudes are consistently underestimated by the model as well. If Sable Island wind underestimates stress over the CASP region, then the observed gains would be overestimated. Wind stress near the coast, where the observed and model gains are similar, is reduced (Smith 1987), so Sable Island wind may be more representative in coastal areas. However, since changes in coastal SSP are associated with the velocity response integrated across the entire shelf, then nearshore and coastal pressure would be underestimated by the model. The role of spatially inhomogeneous wind forcing is an area worth examining with future models. Theoretical work by Chapman (1987) shows that model predictions are most sensitive to the quality of wind stress forcing.

Alternatively, the bottom friction coefficient (r) may be wrong or improperly parameterized. Flow increases when the value of r is reduced (Haidvogel and Brink 1986) or varies inversely with depth (cf. Hopkins and Dieterle 1983; Chapman et al. 1986). As noted previously, however, sensitivity studies with the model used here indicate that current speed is relatively unaffected (less than 20%) by realistic changes in r. Another possibility is that the model grid smooths out details in the true bottom and coastline that may produce locally stronger currents.

4. Model results for nonlocal forcing: Coastally trapped waves?

a. Response to an incident CTW at the backward boundary

The circulation induced by a single-mode periodic CTW propagating across the backward boundary (y = 150 km) is described in this section. Again results are compared at ω = 0.125 and 0.438 cpd. The structures of the incident mode 1 and 2 CTWs at the backward boundary are shown in Fig. 10. To be consistent with the statistical results from Schwing (1992), transport is calculated from the pressure field normalized by Louisbourg SSP (y = 0) and is expressed in units of $m^2\ s^{-1}/m$. Transport phase is also set relative to Louisbourg SSP. Vectors in the region east of Louisbourg have been omitted for clarity.

The mode 1 contribution to Scotian Shelf circulation at 0.125 cpd (Fig. 11) is steered around shallow areas, resulting in quiescent regions over Sable Island Bank and near the coast. To compensate, transport increases through the deeper areas of the shelf. This is opposite the locally forced response (Fig. 3), where flow is stronger in shallower areas. A substantial amount of the flow is deflected offshelf and against the incident transport by Sable Island Bank. Transport decreases in magnitude in the forward direction, probably because of wave scattering by irregular bathymetry and strong bottom stress over shallow regions. The SSP in the CASP region lags Louisbourg SSP by about 10°, and is approximately out of phase with local transport.

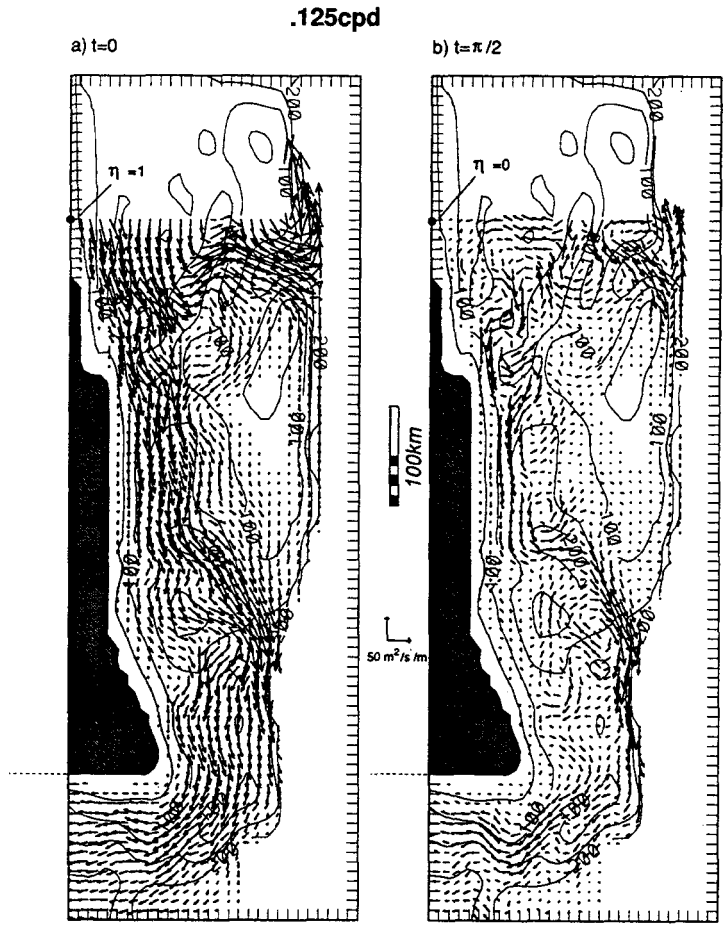

FIG. 11. Model transport, forced at backward boundary (y = 150 km) by mode 1 CTW periodic at 0.125 cpd, at (a) $t = 0$ and (b) $t = \pi/2$. Vector lengths are normalized by Louisbourg SSP; units are $m^2\ s^{-1}$/Pa. Transport in region $0 < y < 150$ km omitted for clarity. White areas forward of origin ($y < 0$ km) denote transport less than 1 $m^2\ s^{-1}$/Pa.

Thus, maximum SSP is nearly coincident with maximum transport in the forward direction, and the resulting current is in geostrophic balance with the cross-shelf gradient, as suggested by Schwing (1992). Transport at $t = \pi/2$ (Fig. 11b), when SSP at the backward boundary and over most of the shelf is falling, especially reflects the complicated flow regime seen in the wind-forced responses. The meandering circulation pattern again is linked closely to bathymetric changes.

As with the wind-forced case, the pattern and magnitude of the remotely forced flow west of Halifax display excellent agreement with the steady numerical solutions of Wright et al. (1986) and Lynch et al. (1992), forced by a coastal SSP setup at Halifax. In particular, all three models show quiescent areas near the coast, and convergence and maximum transport northwest of Browns Bank. Current speeds are similar in the region common to these models, as well.

A rather surprising model result is that the nonlocal circulation off Nova Scotia is *independent of the incident wave form* applied at the backward boundary. The solution forced by a mode 2 CTW displays a nearly identical circulation pattern to that shown in Fig. 11. The only major difference is an increased phase lag to the mode 2 wave of about 60°. This increased lag is nearly constant over the entire domain; thus, phase differences forward of Louisbourg are essentially identical for either mode. The similarity of this response, and its possible mechanism, is demonstrated in Fig. 12, which compares the amplitude of the pressure field, normalized by Louisbourg SSP, for the mode 1 and 2 incident CTWs.

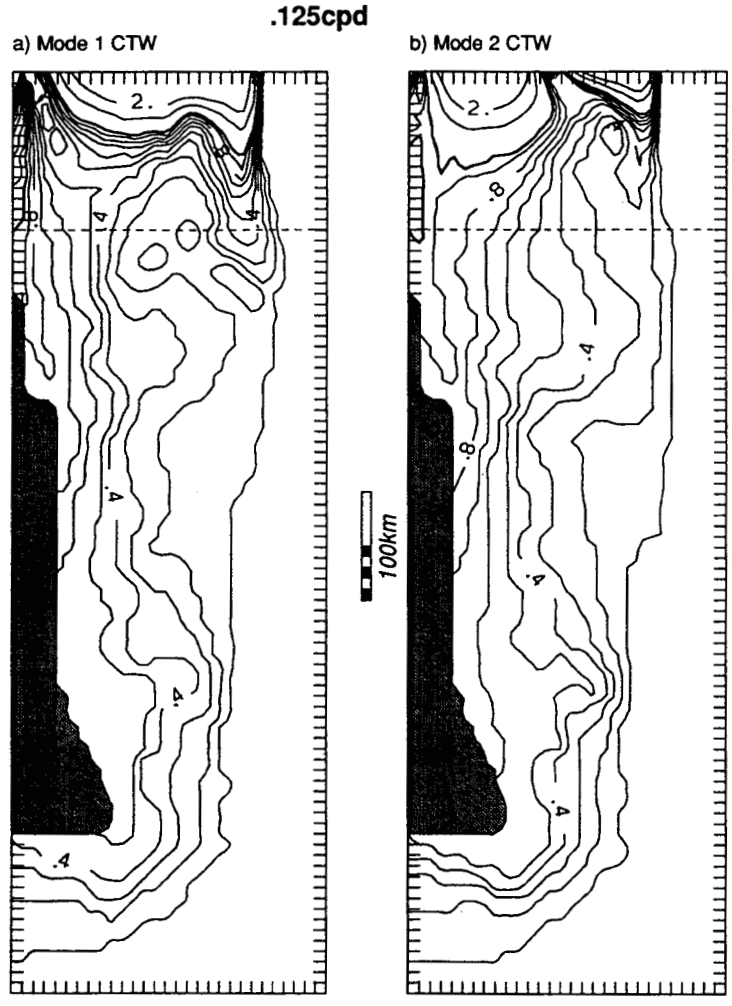

FIG. 12. Amplitude of SSP field, forced by (a) mode 1 and (b) mode 2 incident CTW at backward boundary. Amplitude normalized to Louisbourg SSP.

The highly irregular bathymetry east of Louisbourg rapidly alters the incident wave structure, resulting in a nearly identical forward-propagating form. This rapid modification is also evident in the cross-shelf modal structure off Louisbourg, particularly at higher frequencies (Fig. 10). The outer-shelf banks seem particularly effective in dissipating and/or scattering and reflecting wave energy. Modal differences in the incident wave are greatest in this region.

The nonlocal response is less restricted to deeper shelf regions at 0.438 cpd (Fig. 13). Mesoscale variations in the flow at $t = 0$ again occur in association with strong bathymetric changes. However, these small-scale features are less pronounced at higher frequencies, a relationship also seen in the idealized CTW model results of Schwing (1989a), as well as in the local wind-forced response described in section 3. Increasing ω decreases the length of the "shadow zone" forward of a bathymetric feature (Wilkin and Chapman 1987). The magnitude of the transport at $t = \pi/2$ is relatively strong, reflecting the greater ($\sim 30°$) phase lag of SSP in the CASP region of the model to Louisbourg.

b. *Comparison with observations*

Model and observed coastal SSP responses to remote forcing show good general agreement (Schwing 1989b). Correlation between the observed and modeled velocity responses will confirm the model's ability to reproduce this relationship on smaller spatial scales. The transfer functions between CASP alongshelf velocity and

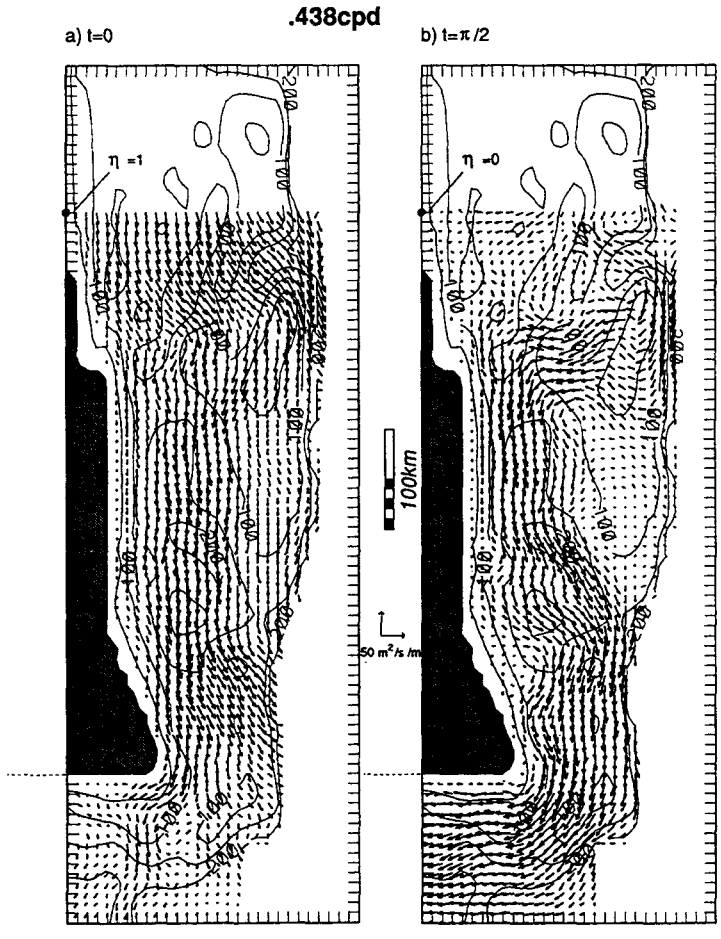

FIG. 13. Model transport, forced at backward boundary by mode 1 CTW periodic at 0.438 cpd, at (a) $t = 0$ and (b) $t = \pi/2$. Vector lengths are normalized by Louisbourg SSP; vector units are $m^2 s^{-1}$/Pa. Transport in region $0 < y < 150$ km omitted for clarity. White areas forward of origin denote transport less than 1 $m^2 s^{-1}$/Pa.

Louisbourg SSP at 0.125 cpd and 0.438 cpd, taken from Schwing (1992), are compared to the mode 1 CTW model results in Fig. 14.

Remotely forced observations are very comparable to model alongshelf velocity and SSP at most stations. Model results replicate observed phase differences to within about 10° in most cases, and match observed gains in the synoptic band as well. As with the wind-forced simulations, however, model velocities at the offshore stations generally underestimate observations at 0.125 cpd, despite the fact that SSP gains are quite similar. Remotely forced geostrophic flow through the Halifax line was estimated from the cross-shelf pressure gradient and the alongshelf velocity response (Schwing 1992). While these independent estimates are reasonably close at higher frequencies, this analysis suggests that the pressure gradient is not large enough to balance the observed alongshelf flow at 0.125 cpd.

The mode 1 wave-forced solution (Fig. 11) exhibits a phase speed of ~ 17 m s^{-1} and a decay scale of ~ 800 km at 0.125 cpd, while these parameters are about 27 m s^{-1} and 1200 km at 0.438 cpd, based on coastal SSP results. Nearly identical values are obtained from the mode 2 results, validating the independence of the flow field from the incident wave structure. The observed exponential decay scale based on coastal SSP is similar (Schwing 1989b, 1992), suggesting that the parameterization of bottom friction is reasonable. The phase speed determined from observed coastal SSP is nearly identical to the model results at 0.438 cpd, but overestimated by a factor of ~ 3 at 0.125 cpd. Of course, these model characteristics vary greatly on small spatial

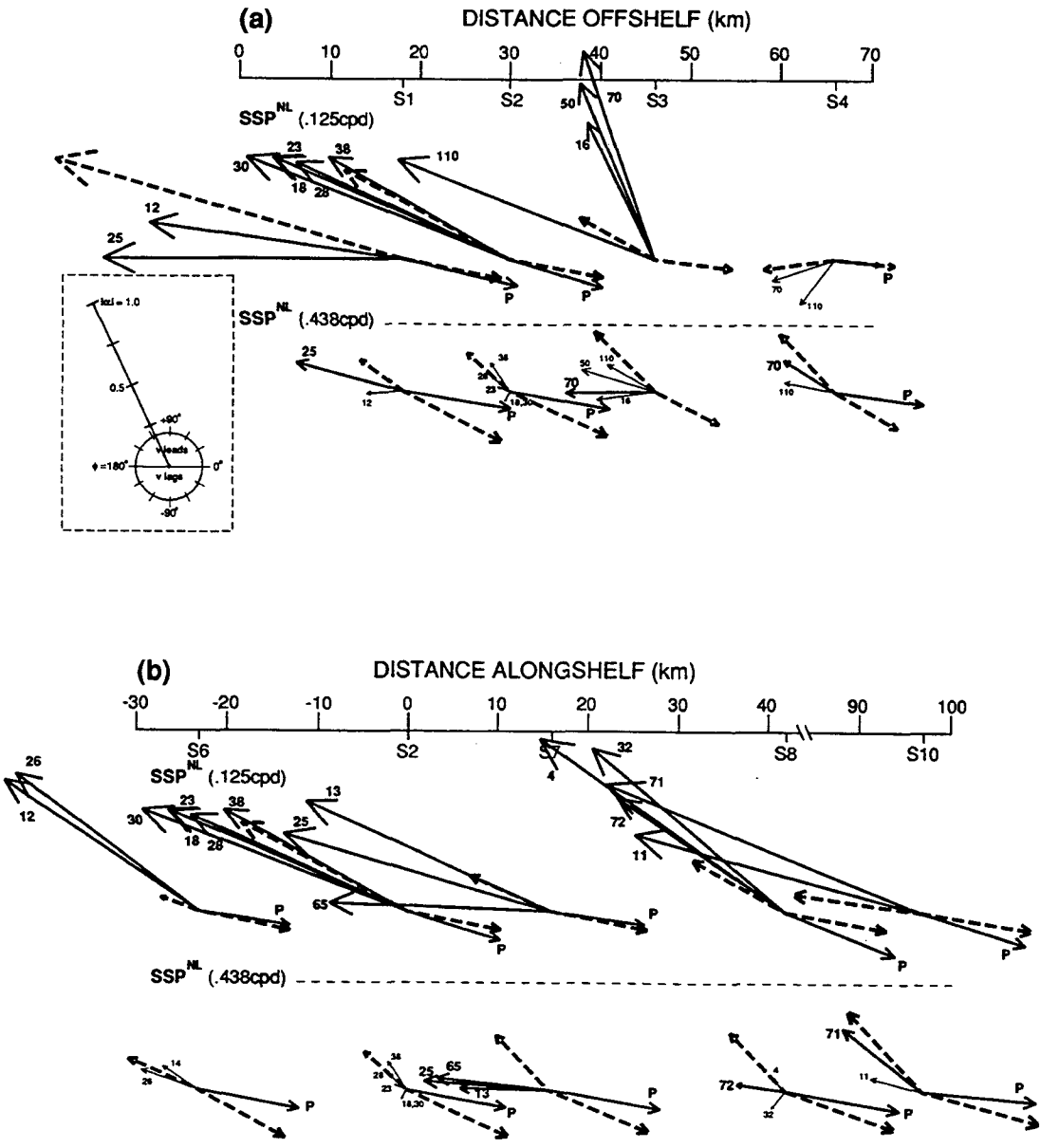

FIG. 14. Comparison of observed and model responses of v to nonlocal forcing at 0.125 and 0.438 cpd, for stations in the (a) Halifax line and (b) 100-m isobath line. Vectors describe amplitude and phase of response. Model results (broken vectors) adapted from Figs. 11 and 13. Observations (solid vectors) based on multiple regression analysis in Schwing (1992); bold vectors denote 95% significance.

scales; the aforementioned values are averaged along the entire shelf.

The discrepancy between observations and the model results supports the idea that the low-frequency circulation includes a strong ageostrophic component. Another possibility is that energy scattered into higher wave modes may add substantially to the total current but contribute little to the SSP signal, which is strongly biased toward the lowest mode (Hsieh 1982). This imbalance also holds true for the observed response to τ^y (Schwing 1992), and thus may partially account for the relatively small model currents in the vicinity of

Emerald Basin. It was also shown that flow at nearshore stations exhibits a response more typical of the integrated circulation. This may explain why model results fit observations better at the nearshore stations.

Of course, baroclinic effects, which may inhibit the scattering or dissipation of higher modes (Chapman 1983), cannot be ruled out as a potentially important source of variability beyond the 100-m isobath. Interaction between the remote response and local wind forcing that was not properly separated by the statistical models is also a possibility. Future modeling efforts of the Scotian Shelf should carefully examine these effects.

5. Discussion and summary

Statistical analysis of the CASP data has defined the important subtidal scales and patterns of the Scotian Shelf circulation (Schwing 1989a,b, 1992). A hierarchy of analytical and numerical models was also developed by Schwing (1989a) to provide a physical basis for understanding what processes may be responsible for the variability observed during CASP. Results from these idealized models indicate that bathymetric irregularities have a profound influence on flow in coastal regions. The primary goal of this paper has been to develop a numerical model of the Scotian Shelf circulation that features realistic bathymetry, whose results could be compared directly to SSP and velocity observations.

The most interesting model result is the presence of several circulation features associated with bathymetric changes. The flow displays a strong tendency to parallel f/h contours where the bathymetry is relatively smooth and bottom gradients are weak. However, closed circulation cells of order 50–100 km in diameter develop over steep bathymetry. The vorticity balance is given by taking the curl of (1)–(2) and substituting for $\nabla \cdot \mathbf{v}$ from (3):

$$\left(\xi - \frac{f}{h}\eta\right)_t - \frac{f}{h}\mathbf{v}\cdot\nabla h - \nabla \times \left(\frac{\tau - r\mathbf{v}}{h}\right) = 0, \quad (12)$$

where $\xi = v_x - u_y$ is the relative vorticity. The first term in (12) is the time rate of change of relative vorticity less the effect of changes in the free surface; the second represents local cross-isobath flow (vortex tube stretching); and the final term is the curl of the surface minus bottom stress.

The inclusion of time dependence has little effect in shallow water, as friction balances vortex stretching. The primary balance is between inertia and stretching in deep water. Over relatively flat regions, (12) is simply

$$\left(\xi - \frac{f}{h}\eta\right)_t = -\frac{r}{h}\xi$$

in the case of a spatially uniform wind, or $\epsilon\xi = 0$ with the rigid-lid approximation. The vorticity balance is between inertia and bottom stress. However, the vortex stretching term becomes large over steep bathymetry. An area of vortex squashing, which creates negative relative vorticity, develops over a region of shoaling bathymetry. Vortex stretching and the resultant generation of positive vorticity occurs over deepening bathymetry. The circulation associated with Emerald Basin, for example, is deflected to the left (right) over the deepening (shoaling) portion of the basin, to balance the generation of positive (negative) relative vorticity. In contrast, no mechanism for generating vorticity exists where the depth is constant.

It is important to note that the bathymetric contribution to the amplitude of the pressure field is not nearly as significant as it is to the magnitude and direction of the current. For the spatial scales typical of the Scotian Shelf, the influence of bathymetry modifies the response of the pressure field by less than 10% of coastal SSP, but increases the transport by as much as a third and changes the direction of the flow on the order of 30° (Schwing 1989a). Given these results, it is not surprising that the observed current patterns on the rugged Scotian Shelf are so incoherent, while SSP is highly correlated over large horizontal separations. Despite the extremely irregular bathymetry of the Scotian Shelf, it is possible to describe the interaction between circulation and bathymetry on relatively small horizontal scales with a properly resolved numerical model and relate observed patterns to fundamental dynamical balances. However, it is obviously not possible to monitor the transient shelf circulation with coastal sea level measurements or a limited array of SSP gauges.

Numerical model results generally reproduce the diverse local and nonlocal velocity responses observed in the CASP data. The model appears most effective at explaining the circulation induced by motions propagating onto the shelf from the east. The amplitude and phase of the observed SSP and velocity responses to nonlocal forcing are nearly identical at most stations (Fig. 14). The exponential decay scales estimated from model and observed SSP are consistent, although the model phase speed differs from that determined from the observations. More significantly, the circulation forward of Louisbourg is *independent* of the incident wave structure at the backward boundary, only 150 km to the east, suggesting that bathymetry rapidly modifies the propagating free signal. Given the extremely rugged shelf bathymetry and the apparently strong influence of bottom stress, it is believed that the incident wave is continuously scattered into higher modes (Wilkin and Chapman 1990) that are dissipated over small horizontal scales (Webster 1985).

The reproduction of the observed variations forced by wind stress over the Scotian Shelf is less successful, although the general circulation patterns within the CASP array are seen in the model results. Discrepancies in the amplitude of the observed and model responses to local wind forcing are noted over the deeper portions

of the shelf, which may be due to mesoscale variability in the wind field. Much of the perceived variability in the direction of flow is due to the depth-integrated aspect of model transport. However, variations in u are difficult to quantify. The ability to adequately describe the cross-shelf flow remains one of the outstanding problems in coastal oceanography.

Some of the discrepancy between the offshore CASP and model circulation, in both local and nonlocal responses, may be associated with baroclinic effects. Baroclinicity undoubtedly influences Scotian Shelf circulation, particularly over the outer portion of the shelf (Petrie 1983). There is, however, some justification for a barotropic model. First, the structure of the shelf water in winter within most of the CASP array and over much of the shelf is well mixed to the bottom (Smith et al. 1978; Schwing 1992). The alongshelf current response during CASP generally does not display the significant depth variability that would be expected in the case of baroclinic flow (Schwing 1992). Anderson and Smith (1989) conclude that the mean circulation is predominantly barotropic. The importance of baroclinic motions is probably limited to near-inertial (Smith 1989) or seasonal time scales. Major variations in the pycnocline position during CASP occurred at periods longer than 10 d, particularly in the near-surface layer and the inner portion of the shelf (Lively 1988). Thus, the baroclinic contribution to the synoptic frequency (barotropic) fluctuations of interest in this study is probably limited to a relatively steady background flow (i.e., the Nova Scotian Current).

Finally, the qualified success with which the model replicates the observed locally and, particularly, remotely generated flow patterns in the shelf region covered by the CASP array implies that much of the circulation may be barotropic. Previous barotropic numerical studies in this region have been instructive (cf. Beardsley and Haidvogel 1981; Wright et al. 1986). However, the potential importance of baroclinicity on the outer shelf must be considered. A natural extension to this work is the application of a stratified model to the Scotian Shelf region.

Perhaps more important, the statistical model results obtained by Schwing (1992) for offshore stations (i.e., S3, S4, S11) generally have large confidence intervals. Thus, the observed responses shown in Figs. 7–9 only approximate the highly variable wind-forced response on the mid- and outer shelf. It may not be possible to say with certainty what contributes to the large flows in deeper water, or even if such fluctuations are caused by meteorological forcing directly over the Scotian Shelf. Given the limited spatial extent of the CASP array, it is impossible to validate the barotropic model results over the outer shelf. In addition, substantial differences in the flow at the resolution of the model mesh mean that imprecise placement of mooring positions within the model domain could lead to some of the poor agreement. Nevertheless, the general compatibility between the observed and model responses to wind forcing gives some credence to the idea that complex shelf circulation features periodic at subtidal frequencies are closely coupled to mesoscale bathymetric variations.

In light of previous theoretical investigations on the effect of idealized and realistic bottom features on circulation, these results are not surprising. The majority of previous studies concerning bathymetric influences have dealt primarily with bathymetric effects on CTWs (Wang 1980; Brink 1986; Wilkin and Chapman 1987, 1990; Middleton and Wright 1988) or some form of remote forcing at the backward boundary (Greenberg and Petrie 1988), although some modeling efforts have examined modifications to the locally forced circulation (cf. Simons 1983; Haidvogel and Brink 1986; Lopez and Clarke 1988).

An early, simple linear barotropic model for the Gulf of Maine (Csanady 1974) showed that closed wind-driven barotropic circulation cells develop over idealized depth gradients, due to the generation of vorticity by stretching. Subsequently, more elaborate and bathymetrically realistic models have been used to study flow–bathymetry interaction (Beardsley and Haidvogel 1981; Wright et al. 1986; Greenberg and Petrie 1988; Lynch et al. 1992). As mentioned previously, the steady solutions of Wright et al. (1986) and Lynch et al. (1992) exhibit the same circulation patterns and scales of variability, and quantitatively agree with the results presented here. While results from a barotropic model of the Newfoundland shelf (Greenberg and Petrie 1988) do not include the closed circulation features seen on the Scotian Shelf, they do exhibit several areas of nonisobathic flow and substantial horizontal shear on the region's small bathymetric scales.

In the Middle Atlantic Bight, forward of the Scotian Shelf, realistic numerical solutions exhibit a generally alongshelf wind-driven flow that increases in amplitude to the south (Beardsley and Haidvogel 1981), and is embedded with numerous small-scale features that are tied to bathymetric variations (Hsueh 1980; Beardsley and Haidvogel 1981; Hopkins and Dieterle 1983). The moving storm experiments of Beardsley and Haidvogel, analogous to the periodic wind-forced solutions described here, also display small-scale and highly transient oscillations and a southward phase propagation. Another general conclusion is that the influence of alongshelf wind stress forcing is much greater than the cross-shelf component.

The inability to replicate the observed velocity is also not unique to this model. Brink et al. (1987) and Chapman (1987) also underestimate actual current speeds. Greenberg and Petrie's (1988) barotropic model underpredicts flow in some areas as well. The reason why many models give systematically low current speeds is not understood and may vary with the physics inherent in each study.

A novel aspect of the numerical model applied here is the separation of solutions into local and remote contributions, using two different forcing fields and backward cross-shelf boundary conditions. The uniquely complex bathymetry is a feature of only select realistic models of the region (Beardsley and Haidvogel 1981; Wright et al. 1986; Lynch et al. 1992), and unmatched by idealized models that often consider simple isolated bathymetric features. The Scotian Shelf proper has not previously been modeled with real bathymetry. The relaxation of the rigid lid allows for the inclusion of the Kelvin wave in solutions, which is shown by Lopez and Clarke (1989) to be an important contributor to the SSP field. Finally, wavelike solutions, which were sought in many earlier models, are not considered here.

Webster (1985) argues that the nonlocal response at a location is due to constructive and destructive interference of CTWs generated over the backward section of the shelf. The number and structure of wave modes contributing to the remote flow is a function of the degree of scattering and reflection of each mode and the importance of bottom stress, which determine the wavelength, frequency, mode number, and decay scale of the waves involved. It appears that higher and short wave modes are selectively dissipated over short length scales, leaving a large-scale flow that is predominated by low-mode, frictionally decaying long waves.

While the general circulation is dominated by low modes, particularly near the coast (Webster 1985), higher-mode and reflected waves may be extremely important in the vicinity of irregular bathymetric features, and may lead to the spatially incoherent flow observed during CASP. This is especially true for velocity as it reflects the structure of the free response more accurately than SSP, which is strongly biased for the lowest mode (Hsieh 1982). The strength and phase of the current varies substantially over short spatial scales in scattering regions (Wilkin and Chapman 1990). For highly idealized bathymetry (i.e., a single feature), solutions can be treated with relatively few wave modes. But the bathymetric length scales on the Scotian Shelf are too short to allow for a reasonable description of the circulation with wavelike solutions. Thus, a modal approach can be very inefficient at representing realistic flows over complex bathymetry.

The similar patterns induced by the mode 1 and 2 incident waves in Figs. 11–13, and similarities between the wind-forced and free solutions, further focus on the ambiguity of wavelike solutions (Brink 1986). A more logical approach is to consider the total circulation to be composed of local and remote influences, as suggested by Gill and Schumann (1974) and others. Lopez and Clarke (1989) show that, without the local response, too many wave modes are required to accurately describe the low-frequency velocity field. The local contribution can be described by a diffusive-like solution analogous to the ATW solution first presented by Csanady (1978), while the remotely generated portion is possibly defined by the familiar modal forms of the CTW theory. However, both contributions are greatly influenced by the local bathymetry, as well as by the bottom structure over which the flow has propagated.

The separation of the "local" and "nonlocal" contributions is an arbitrary one, dependent upon the position of the backward boundary. This is because pressure or current at any location is a continuum of propagating signals, each generated by wind forcing somewhere backward from that point, and continually modified by additional variations in surface and bottom stress and bathymetry. The striking coherence between the circulation driven by direct wind stress forcing over the region of interest (Figs. 2–8) and CTWs propagating from a distant source (Figs. 11–13) dramatically demonstrates this. It also further strengthens the argument for dynamical models that combine local and remote effects, rather than seek modal solutions or consider only local wind forcing. The key to the success of this approach is properly selecting a physically reasonable position for the backward boundary (e.g., the eastern edge of the shelf).

While this study has highlighted the importance of local and remote forcing and the interaction between flow and bathymetry, it also has set the stage for further investigations. Although observed and modeled results suggest that baroclinic and nonlinear motions during CASP are minor (Schwing 1989a), such effects should be considered in future models. Variability in the flow due to, and on the scales of, spatial inhomogeneities in the wind field have not been considered here. Smith (1989) stresses the need to define the mesoscale wind field to model inertial waves accurately. The numerical model developed here can be modified easily to examine the role of wind curl in subtidal motions as well.

Finally, while the significance of remotely generated motions has been demonstrated, their source is unknown. Is there an energy flux across the Laurentian Channel, or out of the Gulf of St. Lawrence? The model results presented here, which demonstrate that bathymetric steering is very strong, imply a gulf origin. Recent theoretical work by Middleton (1991) suggests that, for the dimensions of the Cabot Strait, a Kelvin wave propagating out of the gulf is the primary source of these motions. Only about 20% of the energy may be due to waves crossing the Laurentian Channel. Wang (1980) has shown that a cross-shelf canyon is an effective energy sink to free waves. However, an incident wave that is long relative to the canyon width should pass over that feature relatively easily (Wang 1980; Middleton and Wright 1988). Obviously, more work is required to verify the source of remote energy.

Results from the CASP meteorological experiment, and an existing knowledge of the typical storm track (Lewis and Moran 1984), have improved the capability for predicting the Scotian Shelf mesoscale wind field.

This will hopefully lead to better estimates of the wind-driven shelf flow. Once the origin of nonlocal energy is known, free motions will become easier to forecast as well. Given the qualitative success of the local and remote models, this raises the intriguing possibility of developing predictive models to detail the subtidal circulation of the Scotian Shelf and other coastal regions. In the interim, it is hoped that the results presented here provide a useful guide for establishing the proper backward boundary condition for Gulf of Maine–Middle Atlantic Bight models, and will serve as a reference point for further model development as well as a base for planning future observational studies on the Scotian Shelf.

Acknowledgments. I am grateful to Drs. Keith Thompson, Peter Smith, Dan Wright, Chris Garrett, Pat Keast, and Ken Brink for their stimulating scientific discussion and critical review during the preparation of this manuscript. I also acknowledge the scientific and logistic support of many individuals at Bedford Institute of Oceanography, particularly Dr. Carl Anderson. This work was supported (in part) by the Federal Panel on Energy R&D (PERD).

APPENDIX A

Finite-Difference Solutions for the Numerical Model

The discretized model domain consists of $(I + 1) \times (J + 1)$ mesh points in the x (cross-shelf) and y (alongshelf) dimensions, respectively (Fig. A1). The continuous variables in x and y are replaced by discrete variables at points i, j, defined by

$$x = i\Delta x \quad i = 0, 1, \cdots, I, \tag{A1a}$$

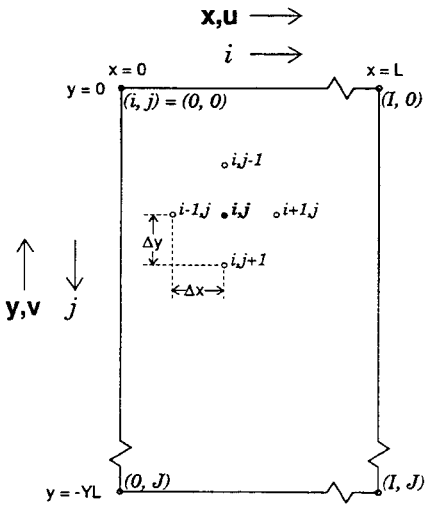

FIG. A1. Schematic showing coordinate system and model domain used in numerical model.

$$y = -j\Delta y \quad j = 0, 1, \cdots, J, \tag{A1b}$$

where Δx and Δy are the finite-difference intervals in the x and y directions, respectively.

The centered space finite-difference form of (7) is

$$p_{i,j}\eta_{i,j} + q_{i,j}\left[\frac{\eta_{i+1,j} - 2\eta_{i,j} + \eta_{i-1,j}}{(\Delta x)^2}\right] + r_{i,j}\left[\frac{\eta_{i+1,j} - \eta_{i-1,j}}{2\Delta x}\right] + s_{i,j}\left[\frac{\eta_{i,j-1} - 2\eta_{i,j} + \eta_{i,j+1}}{(\Delta y)^2}\right] + t_{i,j}\left[\frac{\eta_{i,j-1} - \eta_{i,j+1}}{2\Delta y}\right] + 0((\Delta x)^2 + (\Delta y)^2) = F_{i,j}, \tag{A2}$$

where

$$p = -\sqrt{-1}\,\frac{\omega}{f}$$

$$q = \frac{a^2\epsilon}{1 + \epsilon^2}$$

$$r = \left(\frac{a^2\epsilon}{1 + \epsilon^2}\right)_x - \left(\frac{a^2}{1 + \epsilon^2}\right)_y$$

$$s = \frac{a^2\epsilon}{1 + \epsilon^2}$$

$$t = \left(\frac{a^2}{1 + \epsilon^2}\right)_x + \left(\frac{a^2\epsilon}{1 + \epsilon^2}\right)_y$$

$$F = \frac{1}{f^2}\left[\left(\frac{\tau^y + \epsilon\tau^x}{1 + \epsilon^2}\right)_x + \left(\frac{\epsilon\tau^y - \tau^x}{1 + \epsilon^2}\right)_y\right].$$

Finite differences are of second-order accuracy, so the total discretization error is $O[(\Delta x)^2 + (\Delta y)^2]$.

Rearranging (A2) in terms of $\eta_{i,j}$, etc., and multiplying through by $(\Delta x)^2$, gives the general equation

$$a_{i,j}\eta_{i+1,j} + b_{i,j}\eta_{i-1,j} + c_{i,j}\eta_{i,j-1} + d_{i,j}\eta_{i,j+1} + e_{i,j}\eta_{i,j} = f_{i,j}, \tag{A3}$$

where

$$a_{i,j} = q_{i,j} + \frac{\Delta x}{2}\,r_{i,j} \tag{A4a}$$

$$b_{i,j} = q_{i,j} - \frac{\Delta x}{2}\,r_{i,j} \tag{A4b}$$

$$c_{i,j} = \delta^2 s_{i,j} + \delta\,\frac{\Delta x}{2}\,t_{i,j} \tag{A4c}$$

$$d_{i,j} = \delta^2 s_{i,j} - \delta\,\frac{\Delta x}{2}\,t_{i,j} \tag{A4d}$$

$$e_{i,j} = (\Delta x)^2 p_{i,j} - 2q_{i,j} - 2\delta^2 s_{i,j} \tag{A4e}$$

$$f_{i,j} = (\Delta x)^2 F_{i,j}, \tag{A4f}$$

and $\delta = \Delta x/\Delta y$, the ratio of mesh spacing. Equation (A3) is a linear system of equations that includes all values of $i = 0, 1, \cdots, I$ and $j = 0, 1, \cdots, J$, given by (A1); it can also be written in matrix notation as $\mathbf{A}\eta = \mathbf{F}$.

Writing (A3) in a fashion consistent with the SOR method (Young 1971, p. 73ff.; Press et al. 1986, pp. 652–659) gives

$$\eta^{*n}_{i,j} = [f_{i,j} - a_{i,j}\eta^{n}_{i+1,j} - b_{i,j}\eta^{n}_{i-1,j} - c_{i,j}\eta^{n}_{i,j-1} - d_{i,j}\eta^{n}_{i,j+1}]/e_{i,j},$$

where $\eta^{*n}_{i,j}$ is an estimate of $\eta_{i,j}$ obtained at each mesh point during the nth iteration. The updated value of $\eta_{i,j}$ after the nth iteration is the weighted average

$$\eta^{n}_{i,j} = \alpha\eta^{*n} + (1 - \alpha)\eta^{n-1}_{i,j}, \qquad \text{(A5)}$$

where $\eta^{n-1}_{i,j}$ is the value of $\eta_{i,j}$ following the previous iteration and α is the relaxation parameter. From (A5), it is apparent the solution has converged when $\eta^{*n}_{i,j} = \eta^{n-1}_{i,j}$; solutions are assumed to have converged when the norm of the differences between the old and updated values reaches some small value. For the model applied here, this is given by

$$\sum_{i=0}^{I}\sum_{j=0}^{J} |(|\eta^{*n}_{i,j}| - |\eta^{n-1}_{i,j}|)| \leq 10^{-5}.$$

The key to the efficiency of SOR is optimizing α. Young (1971) provides detailed descriptions of algorithms that locate an optimal α, based on a knowledge or estimate of the spectral radius ρ. One such method, used in this work, is Chebyshev acceleration (Press et al. 1986, p. 658):

$$\alpha = 1, \qquad n = 1$$

$$\alpha = \left(1 - \frac{\rho^2}{2}\right)^{-1}, \qquad n = 2$$

$$\alpha = \left(1 - \frac{\alpha\rho^2}{4}\right)^{-1}, \qquad n > 2$$

$$\alpha \to \alpha_{\text{optimal}}, \qquad n \to \infty.$$

Initially setting $\alpha = 1$, α is adjusted after each iteration until the optimum asymptotic relaxation parameter is reached. This acts to improve the average rate of convergence, since the norm of the error always decreases with each iteration. Young (1971) relates methods for estimating ρ.

APPENDIX B

Analytical Solutions for Frictional CTWs at the Backward Boundary

To obtain analytical solutions for a single-mode CTW forcing the remote models through the backward cross-shelf boundary (section 4), three modifications are made. First, the bathymetry at $y = 150$ km is of the exponential form $h(x) = h_1 \exp[2b(x - L_1)]$ from the coast to the shelf break ($x = L_1$), and constant ($h = h_1$) seaward to the outer alongshelf boundary. A constant Rayleigh damping coefficient $\lambda = r/h_0$ is applied to the equations of motion (1)–(2). Finally, the rigid-lid approximation is made in the continuity equation (3) so that a transport streamfunction ψ can be defined, where $\psi_x = vh$ and $\psi_y = -uh$. These modifications allow the vorticity equation

$$-i\epsilon\left[\left(\frac{\psi_x}{h}\right)_x + \left(\frac{\psi_y}{h}\right)_y\right] = \left(\frac{\psi_y}{h}\right)_x - \left(\frac{\psi_x}{h}\right)_y \qquad \text{(B1)}$$

to be derived from (1)–(3). The Rayleigh form of friction in (B1) means that

$$\epsilon = \left(i\frac{\dot{\omega}}{f} + \frac{\lambda}{f}\right)$$

is a constant.

Solutions to (B1) are assumed to be of the separable, periodic form

$$\psi = \phi(x)\exp[i(\omega t - ly)], \qquad \text{(B2)}$$

where ω is the frequency and $l^{\pm} = l_{\mathcal{R}}^{\pm} \pm il_{\mathcal{I}}^{\pm}$ is the complex wavenumber. Exponential bathymetry, Rayleigh damping, and the rigid-lid approximation allow (B1) to be solved as a second-order ordinary differential equation with constant coefficients, expressed as

$$\phi'' - 2b\phi' - (2ibl\epsilon^{-1} + l^2)\phi = 0. \qquad \text{(B3)}$$

The inviscid limit of (B3) reduces to an equation commonly used to determine the cross-shelf modal structure of frictionless shelf waves (cf. Wilkin and Chapman 1987; Middleton and Wright 1988).

The inclusion of a wall at the coastal and outer shelf boundaries requires

$$\psi = 0 \quad x = 0, L,$$

which allows solutions to (B3) to be simplified to the form

$$\phi = e^{bx}\sin(mx), \qquad \text{(B4)}$$

where $m = n\pi$ for the nth wave mode. Thus, the cross-shelf amplitude of the wave is solely a function of the mode number and bathymetric scale, and is independent of frequency and wavenumber. Dispersion curves and solutions for these conditions are very similar to those for the case of a finite-depth ocean replacing the offshore wall condition (Wilkin and Chapman 1987).

Equations (B3)–(B4) give the dispersion relation for this problem:

$$b^2 + l^2 + m^2 + 2ibl\epsilon^{-1} = 0. \qquad \text{(B5)}$$

Given b, m, and ϵ, it is possible to solve for the roots of l from (B5):

$$l^{\pm} = -b\epsilon^{-1}[1 \pm (1 - \epsilon^2(1 + m^2/b^2))^{1/2}],$$

where l^+ propagates energy in the $+y$ direction (the short wave) and l^- in the $-y$ direction (the long wave). The wavelength of l is $2\pi l_R^{-1}$ and its exponential decay scale is $|l_I^{-1}|$, with the sign of l_I^{-1} denoting the direction in which the wave decays.

REFERENCES

Anderson, C., and P. C. Smith, 1989: Oceanographic observations on the Scotian Shelf during CASP. *Atmos.–Ocean,* **27,** 130–156.

Beardsley, R. C., and D. B. Haidvogel, 1981: Model studies of the wind-driven transient circulation in the Middle Atlantic Bight. Part I: Adiabatic boundary conditions. *J. Phys. Oceanogr.,* **11,** 355–375.

Brink, K. H., 1986: Scattering of long coastal-trapped waves due to bottom irregularities. *Dyn. Atmos. Oceans,* **10,** 149–164.

——, D. C. Chapman, and G. R. Halliwell, Jr., 1987: A stochastic model for wind-driven currents over the continental shelf. *J. Geophys. Res.,* **92,** 1783–1797.

Chapman, D. C., 1983: On the influence of stratification and continental shelf and slope topography on the dispersion of subinertial coastally trapped waves. *J. Phys. Oceanogr.,* **13,** 1641–1652.

——, 1987: Application of wind-forced, long, coastal-trapped wave theory along the California coast. *J. Geophys. Res.,* **92,** 1798–1816.

——, J. A. Barth, R. C. Beardsley, and R. G. Fairbanks, 1986: On the continuity of mean flow between the Scotian Shelf and the Middle Atlantic Bight. *J. Phys. Oceanogr.,* **16,** 758–772.

Csanady, G. T., 1974: Barotropic currents over the continental shelf. *J. Phys. Oceanogr.,* **4,** 357–371.

——, 1978: The arrested topographic wave. *J. Phys. Oceanogr.,* **8,** 47–62.

——, 1980: Longshore pressure gradients caused by offshore wind. *J. Geophys. Res.,* **85,** 1076–1084.

——, 1982: *Circulation in the Coastal Ocean.* D. Reidel, 279 pp.

Gill, A. E., and E. H. Schumann, 1974: The generation of long shelf waves by the wind. *J. Phys. Oceanogr.,* **4,** 83–90.

Greenberg, D. A., and B. D. Petrie, 1988: The mean barotropic circulation on the Newfoundland shelf and slope. *J. Geophys. Res.,* **93,** 15 541–15 550.

Haidvogel, D. B., and K. H. Brink, 1986: Mean currents driven by topographic drag over the continental shelf and slope. *J. Phys. Oceanogr.,* **16,** 2159–2171.

Hopkins, T. S., and D. A. Dieterle, 1983: An externally forced barotropic circulation model for the New York Bight. *Contin. Shelf Res.,* **2,** 49–73.

Hsieh, W. W., 1982: On the detection of continental shelf waves. *J. Phys. Oceanogr.,* **12,** 414–427.

Hsueh, Y., 1980: On the theory of deep flow in the Hudson Shelf valley. *J. Geophys. Res.,* **85,** 4913–4918.

Lewis, P. J., and M. D. Moran, 1984: Severe storms off Canada's East Coast: A catalogue summary for the period 1957 to 1983. Canadian Climate Centre, Rep. No. 84-13, Atmosphere Environmental Service, Downsview, Ontario, 345 pp.

Lively, R. R., 1988: Current Meter, Meteorological, Sea-Level and Hydrographic Observations from the CASP Experiment, off the Coast of Nova Scotia, November 1985 to April 1986. Can. Tech. Rep. Hydrogr. Ocean Sci., No. 100, vii + 428 pp.

Lopez, M., and A. J. Clarke, 1989: The wind-driven shelf and slope water flow in terms of a local and a remote response. *J. Phys. Oceanogr.,* **20,** 1091–1101.

Lynch, D. R., F. E. Werner, D. A. Greenberg, and J. W. Loder, 1992: Diagnostic model for baroclinic, wind-driven and tidal circulation in shallow seas. *Contin. Shelf Res.,* **12,** 37–64.

Middleton, J. F., 1991: Coastal-trapped wave scattering into and out of straits and bays. *J. Phys. Oceanogr.,* **21,** 681–694.

——, and D. G. Wright, 1988: Shelf wave scattering due to a longshore jump in topography. *J. Phys. Oceanogr.,* **18,** 230–242.

Petrie, B. D., 1983: Current response at the shelf break to transient wind forcing. *J. Geophys. Res.,* **88,** 9567–9578.

Press, W. H., B. P. Flannery, S. A. Teukolsky, and W. T. Vetterling, 1986: *Numerical Recipes.* Cambridge University Press, 818 pp.

Ramp, S. R., R. J. Schlitz, and W. R. Wright, 1986: The deep flow through the Northeast Channel, Gulf of Maine. *J. Phys. Oceanogr.,* **15,** 1790–1808.

Schwing, F. B., 1989a: Subinertial circulation on the Scotian Shelf: Observations and models. Ph.D. dissertation, Dalhousie University, Halifax, N.S., Canada, 206 pp.

——, 1989b: Subtidal response of the Scotian Shelf bottom pressure field to meteorological forcing. *Atmos.–Ocean,* **27,** 157–180.

——, 1992: Subtidal response of the Scotian Shelf circulation to local and remote forcing. Part I: Observations. *J. Phys. Oceanogr.,* **22,** 523–541.

Simons, T. J., 1983: Resonant topographic response of nearshore currents to wind forcing. *J. Phys. Oceanogr.,* **13,** 512–523.

Smith, P. C., 1987: The distribution of surface wind over the Scotian Shelf. *Proc. Int. Workshop on Wave Hindcasting and Forecasting,* Halifax, Nova Scotia. Environmental Revolving Funds, Rep. Ser. No. 065, 25–36.

——, 1989: Inertial oscillations near the coast of Nova Scotia. *Atmos.–Ocean,* **27,** 181–209.

——, B. Petrie, and C. R. Mann, 1978: Circulation, variability and dynamics on the Scotian Shelf and Slope. *J. Fish. Res. Board Can.,* **35,** 1067–1083.

Vermersch, J. A., R. C. Beardsley, and W. S. Brown, 1979: Winter circulation in the western Gulf of Maine: Part 2. Current and pressure observations. *J. Phys. Oceanogr.,* **9,** 768–784.

Wang, D.-P., 1980: Diffraction of continental shelf waves by irregular alongshore geometry. *J. Phys. Oceanogr.,* **10,** 1187–1199.

Webster, I., 1985: Frictional continental shelf waves and the circulation response of a continental shelf to wind forcing. *J. Phys. Oceanogr.,* **15,** 855–864.

——, and S. Narayanan, 1988: Low-frequency current variability on the Labrador Shelf. *J. Geophys. Res.,* **93,** 8163–8173.

Wilkin, J. L., and D. C. Chapman, 1987: Scattering of continental shelf waves at a discontinuity in shelf width. *J. Phys. Oceanogr.,* **17,** 713–724.

——, and ——, 1990: Scattering of coastal-trapped waves by irregularities in coastline and topography. *J. Phys. Oceanogr.,* **20,** 396–421.

Wright, D. G., D. A. Greenberg, J. W. Loder, and P. C. Smith, 1986: The steady-state barotropic response of the Gulf of Maine and adjacent regions to surface wind stress. *J. Phys. Oceanogr.,* **16,** 947–966.

Young, D. M., 1971: *Iterative Solution of Large Linear Systems.* Academic Press, 570 pp.